Structural Basis for Gating Pore Current in Periodic Paralysis

Daohua Jiang[1,*], **Tamer M. Gamal El-Din**[1,*], **Christopher Ing**[2], **Peilong Lu**[1,3], **Régis Pomès**[2], **Ning Zheng**[1,4,†], **William A. Catterall**[1,†]

[1]Department of Pharmacology, University of Washington, Seattle, WA 98195 USA

[2]Molecular Medicine, Hospital for Sick Children Toronto, ON, Canada M5G 0A4 and Department of Biochemistry, University of Toronto, Toronto, ON, Canada M5G 0A4

[3]Institute for Protein Design, University of Washington, Seattle, WA 98195 USA

[4]Howard Hughes Medical Institute, University of Washington, Seattle, WA 98195 USA

Abstract

Potassium-sensitive Hypokalemic and Normokalemic Periodic Paralysis (HypoPP, NormoPP) are inherited skeletal muscle diseases characterized by episodes of flaccid muscle weakness[1,2]. They are caused by mutations in one gating charge in an S4 transmembrane segment in the voltage sensor (VS) of voltage-gated sodium channel $Na_v1.4$ or calcium channel $Ca_v1.1$[1,2]. Mutations of the outermost arginine gating charges (R1 and R2) cause HypoPP[1,2] by creating a pathogenic gating pore in the VS through which cations leak in the resting state[3,4]. Mutations of the third arginine gating charge (R3) cause NormoPP[5] owing to cationic leak in activated/inactivated states[6]. Here we present high-resolution structures of these pathogenic gating pores in the model bacterial sodium channel Na_VAb[7,8]. Mutation of R2 in Na_VAb gives gating pore current in resting states, whereas mutation of R3 gives gating pore current in activated/inactivated states. Mutations R2G and R3G have no effect on backbone structures of VS, but create aqueous space near the hydrophobic constriction site (HCS) that controls gating charge movement through VS. The R3G mutation extends the extracellular aqueous cleft completely through the activated VS. Although the R2G mutation does not create a continuous aqueous pathway in the activated state, molecular modeling of the resting state reveals a complete water-accessible pathway. Crystal structures of $Na_VAb/R2G$ in complex with guanidinium define a potential drug target site. Molecular dynamics simulations illustrate the mechanism of Na^+ permeation through the mutant gating pore in concert with conformational fluctuations of gating charge R4. Our results reveal pathogenic mechanisms

---

of periodic paralysis at the atomic level and suggest designs of drugs that may prevent ionic leak and provide symptomatic relief from these episodic diseases.

$Na_V1.4$ channels generate action potentials that initiate muscle contraction[9]. They are complexes of pore-forming α and auxiliary $\beta1$ subunits[9–11]. The α subunit contains four homologous domains (I-IV) with six transmembrane segments (S1-S6). Segments S1-S4 form the VS, with positively charged residues at every third position in the S4 segment. Upon depolarization, S4 moves outward through a narrow gating pore formed by S1-S3, catalyzed by exchange of interactions with negative/polar residues in S2 and S3[12]. The VS has an hourglass shape, with a narrow HCS separating extracellular and intracellular compartments[6,11]. Water-filled crevices on either side of the HCS focus the membrane electric field, assuring efficient coupling of voltage to conformational changes that open the central pore[12,13]. Mutations in the arginine gating charge that fills the HCS cause a state-dependent cation leak through the VS, which we term 'gating pore current'[14,15].

Missense mutations in S4 arginine gating charges of $Na_V1.4$ cause HypoPP and NormoPP[1,2,16,17]. Mutations of R1 in domains I or III to H/Q or R2 in domains I, II, and III to W/G/Q/S cause HypoPP[1,2,16,17]. Mutations of R3 in domain II to G/Q/W, or R3 in domain III to H/C cause NormoPP[4,16,17]. All these mutations create non-selective gating pore current through the VS[3,4,16–19]. Increased inward leak leads to Na^+ overload, sustained depolarization, and action potential failure, which paralyzes skeletal muscles[3,16–19]. These pathophysiological effects predict that HypoPP mutations would cause an open aqueous pathway for ion movement through the resting state of the VS, but not the activated state, whereas NormoPP mutations would cause an open aqueous pathway in the activated state, but not the resting state. Molecular models and mutagenesis studies support this idea[20–22]. To provide direct structural evidence for this pathophysiological mechanism, we introduced periodic-paralysis mutations into Na_VAb, whose structure has been solved at high resolution[6,7] and analyzed by molecular dynamics (MD)[23]. We characterized the resulting gating pore currents, solved the structures of mutant gating pores without and with a permeant ion bound, and investigated MD of ion movement through pathogenic gating pores.

To reconstitute pathogenic HypoPP gating pore current in Na_VAb, we mutated R2 to Ser (R2S, analogous to $Na_V1.4$/R672S) and expressed the mutant in *Trichopulsia ni* insect cells. Transfected cells were voltage-clamped to −200 mV and depolarized in 10-mV steps to record Na^+ currents. Half-maximal central pore currents were observed at $V_{1/2}$= −105 ± 0.6 mV (Fig. 1a). To measure gating pore currents, cells were held at −100 mV, where Na_VAb is in the slow-inactivated state and no central pore current is seen. Gating pore current was examined by applying pulses from +100 to −200 mV in −10 mV steps. A nonlinear component of leak current was observed in the resting state, beginning at −110 mV and increasing to −200 mV (Fig. 1b, c).

Mutations of the R3 gating charge that cause NormoPP ($Na_V1.4$/R675G/Q/W) induce outward gating pore current in activated but not in resting states[6]. Na_VAb/R3G central pore current activated from −50 mV to 0 mV (Fig. 1d; V_a=−24.8 ± 1.1 mV). Steady-state inactivation was observed from −90 mV to −10 mV (Fig. 1d; V_h=−47.7±0.4 mV).

Na$_V$Ab/R3G conducted outward gating pore current in activated/inactivated states at potentials more positive than −60 mV (Fig. 1e, f). These physiological studies demonstrate that Na$_V$Ab provides an accurate model of Na$_V$1.4, because gating pore current is observed only in the resting state for R2S and only in the activated state for R3G.

The pathogenic effects of gating pore mutations depend on inward leak of Na$^+$. The R2S gating pore was not significantly selective among Cs$^+$, K$^+$, or Na$^+$ (Fig. 1g). As for Na$_V$1.4[24], guanidinium was exceptionally permeant in the gating pore of Na$_V$Ab/R2S, with a ratio of P$_{Gua}$:P$_{Na}$ ~28. Methylguanidine and ethylguanidine were less permeant (Fig. 1g). The ion selectivity of the outward gating pore current conducted by Na$_V$Ab/R3G was Cs$^+$>K$^+$~Na$^+$ (Fig. 1h). However, the permeation of guanidinium was less than Na$^+$ in Na$_V$Ab/R3G and >40-fold less than in Na$_V$Ab/R2S (Fig. 1h). The weak selectivity among inorganic cations for R2S and R3G and the high guanidinium permeability through R2S are characteristic of corresponding mutations in Na$_V$1.4[2], further supporting Na$_V$Ab as a valid model for structural studies of gating pore mutations.

To elucidate the structure of a pathogenic gating pore in its conductive conformation in an activated VS, we solved the structure of the NormoPP analog Na$_V$Ab/R3G at 2.7 Å resolution (Fig. 2). Na$_V$ channels have a central pore module surrounded by four symmetrically located VS (Fig. 2a). The VS of Na$_V$Ab and Na$_V$1.4 are very similar in amino acid sequence and structure (Extended Data Figs. 1 and 2). Na$_V$Ab/WT and Na$_V$Ab/R3G VS crystallize in the same conformation, with Cα RMSD of 0.39 Å (Fig. 2b, Extended Data Fig. 3). These results indicate that R3G does not perturb VS structure and must therefore have its pathogenic effects because of loss of the R3 side chain. These channels crystallize with activated VS (Fig. 2c)[6,7], as expected at 0 mV. In Na$_V$Ab/WT, R1, R2, and R3 are located extracellular to the HCS, and their sidechains point upward toward the extracellular milieu (Fig. 2c). In contrast, the R4 is located intracellular to the HCS and its sidechain points downward toward the cytosol (Fig. 2c). When viewed from the extracellular side, there is no water-accessible pathway leading inward through the WT VS (Fig. 2d), but we observed a deep solvent-accessible cleft in Na$_V$Ab/R3G extending down to the R4 sidechain (Fig. 2g).

Analysis of the structure of Chain B of Na$_V$Ab/WT using the MOLE2 algorithm revealed an incomplete water-accessible pathway extending part way through the VS from the extracellular and intracellular sides, but interrupted at the HCS by R3 (Fig. 2e). Remarkably, the water-accessible pathway continues all the way through the VS in Na$_V$Ab/R3G, with 2Å diameter at its narrowest point, similar to the size of Na$^+$ (Fig. 2h). In contrast, for Chain A, R4 was captured in a different rotamer conformation in which the arginine sidechain partially blocks the inner end of the gating pore in Na$_V$Ab/R3G (Extended Data Fig. 4a). Our previous structures of Na$_V$Ab in the slow-inactivated state captured R4 in four slightly different rotamer conformations, with the most open having a diameter of 3Å (Extended Data Fig. 4b)[25]. These results elucidate the molecular mechanism through which S4 mutations cause pathogenic gating pore current and further suggest that ion permeation through the gating pore is controlled dynamically by the state of the VS and by rotamer conformations of R4.

In contrast to NormoPP, HypoPP mutants conduct gating pore current in the resting state, and their gating pore is closed in the activated state (Fig. 1). Therefore, we hypothesized that Na$_V$Ab/R2G would not have a continuous water-accessible pathway through its gating pore in the activated state. At 2.9 Å resolution, the structure of R2G revealed a gap with extra solvent-accessible area in the extracellular aqueous cleft but no change in the backbone conformation (Fig. 3a, Extended Data Fig. 3). Although the increased opening of the aqueous cleft in the VS is evident in spacefilling models (Fig. 3b), the R3 and R4 sidechains seal the VS in this activated state, interrupting the transmembrane pathway and preventing ion conductance. The solvent accessible area is ~21 Å deep from extracellular side (Fig. 3c), more than 7 Å deeper than Na$_V$Ab/WT (Fig. 2e), but it does not penetrate through to the cytosolic side. This structure illustrates why Na$_V$Ab/R2G does not conduct gating pore current in the activated state (Fig. 1)

There are no crystal structures of a Na$_V$ VS in its resting state, because the resting state is only accessible at negative membrane potentials. However, we developed models of three resting states from disulfide-locking of substituted cysteine residues and structure prediction with the Rosetta algorithm[26], which are consensus models of the actual resting states[27,28]. For a first glimpse of an open gating pore in the resting state of the VS, we introduced the R2G and R3G mutations into these resting state models and analyzed the resulting structures with the MOLE2 algorithm (Fig. 3d–f). The WT structure does not have a continuous transmembrane pathway through the VS (Fig. 3d), whereas the resting state of the Na$_V$Ab/R2G VS does indeed have a continuous water-accessible pathway (Fig. 3e). Loss of the sidechain of R2 leaves a gap at the HCS that is large enough for permeation of Na$^+$ (Fig. 3e). In contrast, the transmembrane pathway is incomplete in Na$_V$Ab/R3G because the R2 sidechain occupies the HCS and blocks permeation (Fig. 3f). These structural models illustrate how HypoPP mutations in the R2 gating charge cause gating pore current in the resting state of the VS.

Guanidinium ions are highly permeant through the mutant gating pore of Na$_V$Ab/R2S, but much less permeant through Na$_V$Ab/R3G (Fig. 1)[24]. They are chemically similar to the distal moiety of the arginine side chain, and guanidine compounds with hydrophobic substituents can block mutant gating pores[24]. We probed our gating pore structures for guanidinium binding sites by soaking Na$_V$Ab/R2G and Na$_V$Ab/R3G crystals with guanidinium and methylguanidinium to determine whether they would bind in place of the missing sidechain of R2 or R3. We did not find guanidinium bound to Na$_V$Ab/R3G. However, crystals of Na$_V$Ab/R2G soaked with guanidinium or methylguanidinium diffracted to 2.7 Å and 2.5 Å resolution, respectively, and unambiguous electron density was observed in place of each R2 side chain (Fig. 3g–i; Extended Data Fig. 5a, b). Bound guanidinium is clearly seen in 2Fo-Fc maps (Fig. 3h). E32 and M29 from S1, N49 from S2, R1 and R3 from S4, together with Q150 from an adjacent subunit form the binding site for guanidinium (Fig. 3i). M29 and R3 serve as a platform to bind guanidinium through two hydrogen bonds (Fig. 3h, i). The carbonyl group of E32 and the carbonyl oxygen of R1 further lock guanidinium in place (Fig. 3h, i). The binding site is flanked by hydrogen bonds from N49 and Q150 that stabilize guanidinium from opposite sides (Fig. 3h, i). The binding site for methylguanidinium is almost identical (Extended Data Fig. 5c, d). These images capture guanidinium bound at a specific site in the closed R2G gating pore. Amino acid

residues responsible for guanidinium binding are highly conserved in $Na_V Ab$, $Na_V 1.4$, and $Ca_V 1.1$ (Extended Data Fig. 1). Because substituted guanidinium ions can block gating pore current without major effects on $Na_V 1.4$ function[24], guanidinium-containing compounds specific for this binding site could possibly be developed by structure-based drug design and used effectively in therapy of HypoPP.

To examine relationships among structural fluctuations of the gating pore, ionic hydration, and Na^+ leakage, we performed MD simulations of WT and R3G VS in a hydrated lipid bilayer (Fig. 4). Multiple unbiased simulation repeats, totaling 30 µs, show that the overall structures are conserved. Analysis of axial distributions of water molecules revealed a narrow region (−5 Å < z < 5 Å), which is more hydrated in R3G than WT owing to volume opened by the mutation (Fig. 4a–c, yellow; P<0.002, see Extended Data Table 2). The average count of water molecules within the HCS was 3.9±0.8 and 5.3±0.4 for WT and R3G, respectively (Fig. 4e). We performed guided simulations to compute the free energy of Na^+ permeation along the principal axis of the VS. When Na^+ was within the HCS, the number of water molecules increased to 8.4±0.3 and 9.0±0.3 for WT and R3G, respectively. The free-energy profile for Na^+ translocation consists of a broad barrier spanning the HCS, centered at Cα of R3. The R3G mutation significantly decreases barrier height from 18±0.8 to 11±1.4 kcal/mol (Fig. 4f). These values are consistent with undetectable gating-pore conductance for WT and an upper limit of ~0.1 pS for R3G[29]. Analysis of ionic coordination shows that, at the extracellular edge of the barrier, the first solvation shell of Na^+ is almost exclusively composed of water, consistent with the hydrophobic nature of the bottleneck in the VS (Fig. 4g). The total coordination number of 5.81±0.02 in bulk water drops to 4.88±0.04 at the peak of the free-energy barrier, suggesting a large penalty for desolvating Na^+ that is partially alleviated by creation of a cavity by removal of the R3 sidechain. Charge-charge repulsion is also likely to contribute substantially to the higher energy barrier to Na^+ permeation in WT, which is reduced by the R3G mutation permitting pathogenic gating pore leakage.

The location of R4 coincides with a secondary shoulder in the free-energy profiles (Fig. 4d, R108), indicating that movement of Na^+ past R4 is not rate-limiting for permeation, even though transit of Na^+ past R4 causes the greatest displacement of water by protein ligands (Fig. 4f). Spontaneous disruption of the R4-E59 salt bridge in 3±1% of simulation frames for WT and R3G opens the inner end of the gating pore with sufficient frequency to support gating pore current (Fig. 4h–j). Na^+ often makes direct contacts with the anionic sidechains of D80 and E56 (Fig. 4g, h), and its movement is coupled to dynamic rearrangements of the R4 salt-bridge network.

Overall, our results provide an unprecedented high-resolution view of functional effects of ion channel mutations that cause periodic paralysis and define the structural basis for pathogenesis in this ion channelopathy. R2G and R3G mutations do not perturb VS backbone structure, arguing against conformational changes in transmembrane alpha helices as the basis for gating pore current. Instead, removal of the positively charged R2 and R3 side chains opens an aqueous gating pore that allows diffusion of Na^+ into the cell, depending on the functional state of the VS. Our structural studies show how this pathogenic gating pore current is gated in resting and activated states by transmembrane movements of

the S4 segment. Although our studies of R2G and R3G mutants lead to a straightforward explanation for their pathogenic gating pore current, HypoPP and NormoPP mutations that substitute large sidechains such as W also cause gating pore current[4,16,17] and may perturb local structure of the VS as they open a pathogenic gating pore.

Our structures reveal the binding pose of a highly permeant ion, guanidinium, in the closed gating pore in the activated VS of Na$_V$Ab/R2G. Substituted guanidinium derivatives can block gating pore current without impairing VS function in Na$_V$1.4[24]. Therefore, our high-resolution structural models may provide molecular templates for design and development of drugs that would mimic guanidinium, block gating pore current, and provide symptomatic relief from periodic paralysis.

METHODS

Electrophysiology

All experiments were done using *Trichoplusia ni* insect cells (High Five Cells, Thermofisher). Molecular biology and patch-clamp measurements were performed as described previously[15,30]. All constructs showed high level expression that enabled us to measure ionic current and gating pore currents 48 h after infection. Whole-cell sodium currents were recorded using an amplifier (Axopatch 200; Molecular Devices) with glass micropipettes (2–4 MΩ). The intracellular pipette solution contained (mM): 35 NaCl, 105 CsF, 10 EGTA, and 10 HEPES, pH 7.4 (adjusted with CsOH). The extracellular solution contained (mM): 140 NaCl, 2 CaCl$_2$, 1.8 MgCl$_2$, and 10 HEPES, pH 7.4 (adjusted with NaOH).

For Na$_V$Ab/R2S, the standard clamp protocol for measuring central pore currents consisted of steps from a holding potential of −200 mV to voltages ranging from −180 to 0 mV in 10 mV steps. For Na$_V$Ab/R3G, cells were held at −160 mV and 10 mV voltage steps ranging from −140 to +50 were applied. A P/−10 or P/−4 leak subtraction protocol was used to subtract linear leak and capacitive currents from holding potentials of −200 or −160 respectively.

To measure gating pore currents in Na$_V$Ab/R2S, cells were held at −200 mV for ~ 1 min to allow recovery from slow inactivation. Then, the cells were held at −100 mV for gating pore current measurements, which inactivates the central pore current. Depolarizing pulses in 10 mV steps were applied from −200 mV up to +50 mV. The intracellular pipette solution contained (mM): 140 CsF, 10 EGTA, and 10 HEPES, pH 7.4 (adjusted with CsOH). The extracellular solution contained (mM): 140 NaCl, 2 CaCl$_2$, 1.8 MgCl$_2$, and 10 HEPES, pH 7.4 (adjusted with NaOH). To test gating pore selectivity for different cations, NaCl was replaced by an equimolar concentration of KCl, CsCl, LiCl, NMDG, or 40 mM guanidinium sulfate/100 mM NMDG, 40 mM methylguanidinium sulfate/100 mM NMDG, or 40 mM ethylguanidinium sulfate/100 mM NMDG.

To measure gating pore currents in Na$_V$Ab/R3G, cells were held at 0 mV for few min to induce slow inactivation. Then 10 mV pulses were applied from −200 mV up to +50 mV. To measure ion selectivity of R3G, the composition of external solution was in (mM): 140

NMDG-MS, 2 CaCl$_2$, 10 HEPES. The intracellular solution contains either 140 mM NaF, 140 mM KF, or 140 mM CsF, in addition to 10 mM HEPES, 10 mM EGTA.

No online leak subtraction protocols were used during measuring gating pore currents. Linear leak subtraction was made offline by generating a linear fit to the I-V curves at voltage ranges +100 mV to 0 mV for Na$_V$Ab/R2S and between –200 mV and 0 mV Na$_V$Ab/R3G. Voltage-clamp pulses were generated and currents were recorded using Pulse software controlling an Instrutech ITC18 interface (HEKA). Data were analyzed using Igor Pro 6.37 software (WaveMetrics).

Protein Purification and Crystallization

R2G, R2S or R3G mutations were introduced into Na$_V$Ab/I217C by site-directed mutagenesis (QuikChange; Agilent) and confirmed by sequencing. Protein was expressed and purified as described [6]. Briefly, recombinant baculovirus was generated by using the Bac-to-Bac system (Invitrogen), and *Trichopulsia ni* cells (High Five Cells, Thermofisher), were infected for protein production. Protein was extracted with 1% digitonin (EMD Biosciences). After centrifugation, the supernatant was agitated with anti-Flag M2-agarose resin (Sigma). Flag resin was washed and eluted with Flag peptide, and the purified protein was analyzed by SDS-PAGE (Extended Data Fig. 6). Purified protein was then loaded onto a Superdex 200 column (GE Healthcare) in 10 mM Tris-HCl pH 8.0, 100 mM NaCl and 0.12% digitonin. The peak fraction was concentrated to ~17 mg ml^{-1} and reconstituted into DMPC:CHAPSO (Anatrace) bicelles. The protein-bicelle preparation was mixed in a 1:1 ratio and set in a hanging-drop vapour-diffusion format over a well solution containing 1.8–2.0 M ammonium sulphate, 100 mM Na-citrate pH 4.8–5.2. Crystals grew to full size in a week. Crystals were cryoprotected in well solution supplemented with 28% glucose (wt/v) in increments of 7% glucose during harvesting. Guanidnium or methyl guanidinium bound crystals were cryoprotected by soaking in the same cryoprotection solution plus 10 mM guanidinium ions. Crystals were plunged into liquid nitrogen for data collection.

Data Collection and Structure Determination

X-ray diffraction data was collected at Advanced Light Source (beamlines BL821 and BL822), and then integrated and scaled with the HKL2000 suite. Both Na$_V$Ab/R2G and Na$_V$Ab/R3G structures were solved by Phaser-MR using Na$_V$Ab (PDB code 3RVY) monomer as searching model. After initial phases, models were refined with PHENIX[31] and manually re-built using COOT[32]. High-resolution density maps clearly shown no side chain density for R2G or R3G. Simulated annealing omit maps were used to confirm the binding of guanidinium ions. The geometries of the final models were verified using MolProbity[33]. All solvent accessible volume analysis in the voltage-sensing modules was generated with MOLE2[34].

Molecular Modeling and Dynamics

Both molecular models of the Na$_V$Ab/WT and Na$_V$Ab/R3G channels were constructed using the Na$_V$Ab/I217C structure (PDB code: 3RVY)[6]. The latter model was generated by substituting R105 by G in all four VSDs. Both systems were embedded in a hydrated 1,2-dimyristoyl-*sn*-glycero-3-phosphatidylcholine (DMPC) bilayer with ~250 mM NaCl for a

total of ~129,000 atoms. Embedding was performed using the alchembed protocol[35] using an equilibrated rectangular CHARMM36 DMPC bilayer patch obtained from the Klauda laboratory website (https://terpconnect.umd.edu/~jbklauda/). The protein, lipids, and ions were modeled with the CHARMM36 all-atom force field[36–38] and water molecules were modeled with TIP3P[39]. NBFIX adjustments were made for Na^+-backbone carbonyl O atom and Na^+-lipid head group interactions[40,41].

All simulations were performed with GROMACS 5.0.6[42]. Electrostatic interactions were calculated using particle-mesh Ewald algorithm[43,44] with a real-space cut-off distance of 1.2 nm, a grid spacing of 0.16 nm, and cubic interpolation. Lennard-Jones interactions were cut off at 1.2 nm. Nonbonded interactions were calculated using Verlet neighbor lists[45]. All simulations were performed at constant temperature (300 K) using the Nosé-Hoover thermostat[46,47] with temperature coupling of 0.5 ps and at constant pressure (1 atm) with the Parrinello-Rahman barostat[48,49] with a time constant of 2 ps, respectively. All chemical bonds were constrained using the LINCS algorithm[50]. The integration timestep was 2 fs.

Because the channel and voltage sensor were initially devoid of water molecules and ions, a protein-restrained equilibration period of 30 ns was used to reduce the systematic sampling bias induced by the initial conditions (10 ns with protein heavy-atom restraints, 10 ns with backbone restraints, and 10 ns with Cα restraints, all with a force constant of 2.39 kcal/mol/Å^2). Unbiased production simulations of fifteen replicas of "WT" and "R3G" systems were conducted for 1,000 ns each, resulting in aggregate sampling of 15 μs for each tetramer (4×15 μs = 60 μs for "WT" and "R3G" voltage sensors).

Simulation snapshots beyond $t = 100$ ns were extracted from unbiased simulations and used as initial conditions for biased simulations, using the entire tetramer. Umbrella sampling[51,52] was used to compute the free energy or potential of mean force (PMF) profile for the movement of Na^+ through voltage sensing domain. The range of the reaction coordinate, −2.0 to 2.0 nm with respect to the center of the hydrophobic constriction, was discretized into ~130 unevenly spaced windows. For each window, biased simulations were initiated with a water molecule exchanged for Na^+ in all four VS. Production simulations were performed for 70–100 ns per window with a harmonic restraining potential force constant of 2.39 kcal/mol/Å^2 and a flat-bottom cylindrical position restraint for all four Na^+ ions simultaneously. The axial position of the permeating Na^+ ion, z, was stored every 10 fs and the data from each of the four voltage sensors were used separately to generate four independent PMF profiles using g_wham[53], enforcing cyclic periodicity of the PMF in the bulk (at $z = -2.5$ nm). The initial 10 ns were excluded from each umbrella sampling run. We report the mean PMF over the four voltage sensors with error bars computed using the standard error of mean over all four PMFs. The total simulation time for a single VS was 11 μs for each tetramer (4×11 μs = ~45 μs for "WT" and "R3G" voltage sensors).

Water occupancy of the voltage sensor was computed by counting the number of water oxygen atoms within a cylinder of radius 8.0 Å. We define the hydrophobic constriction center as the geometric center of Cα atoms of residues 22, 57, 84, and 105. The range of the HCS is defined as −5 Å to 5 Å along the axial coordinate of the VS. Coordination of Na^+ to channel ligands, water, ions, and lipids was performed by computing the number of protein,

water, and lipid O atoms, as well as Cl^- ions, within the first solvation shell of Na^+ (< 3.0 Å). The average coordination number at a given axial position was computed over all simulation frames regardless of the subunit, but the total coordination number in bulk water and at the hydrophobic constriction reported in the text was based on the mean and standard error of mean over the four voltage sensors. Analysis of the trajectories was performed using MDTraj[54] and molecular renderings were generated using Visual Molecular Dynamics[55].
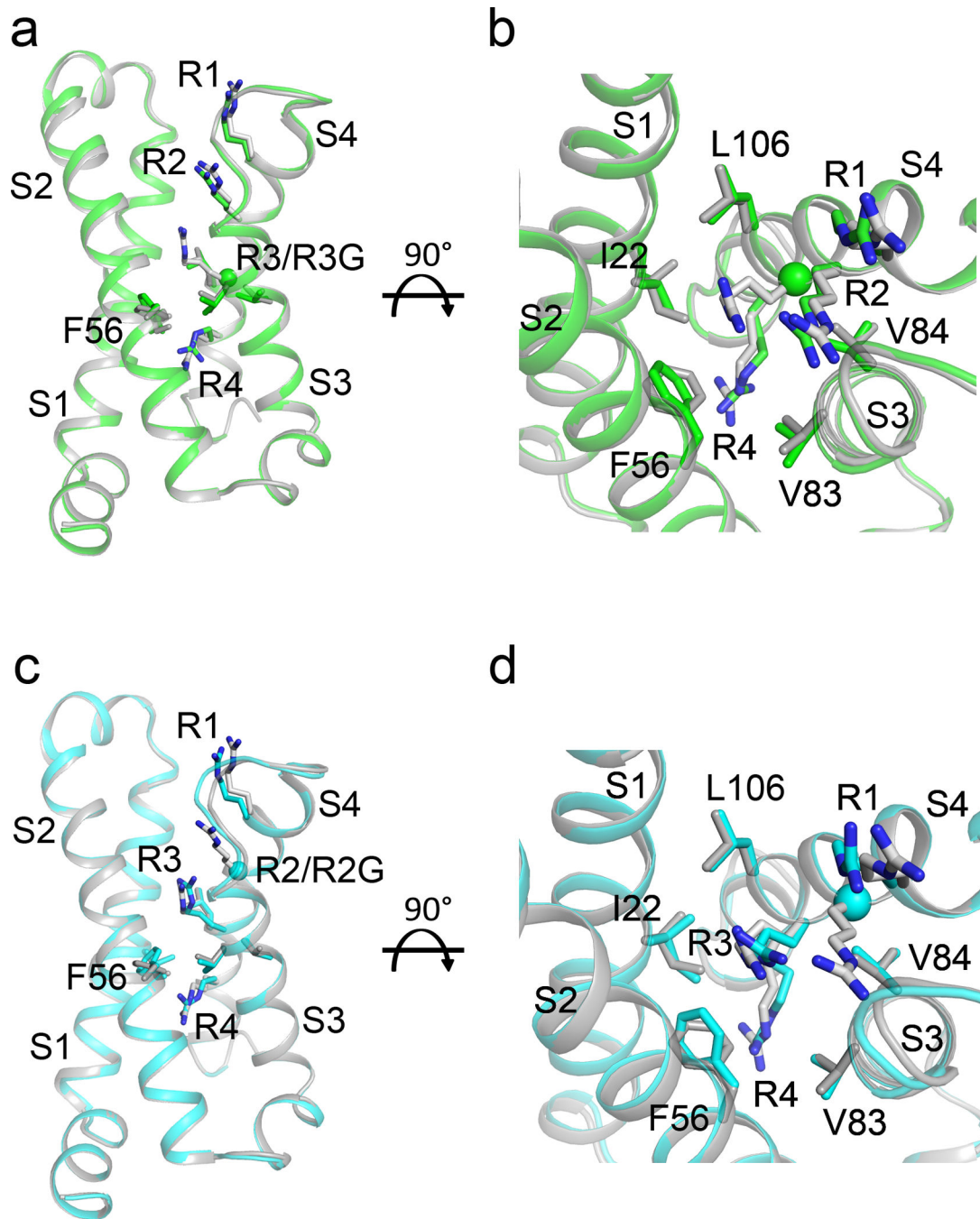
Extended Data
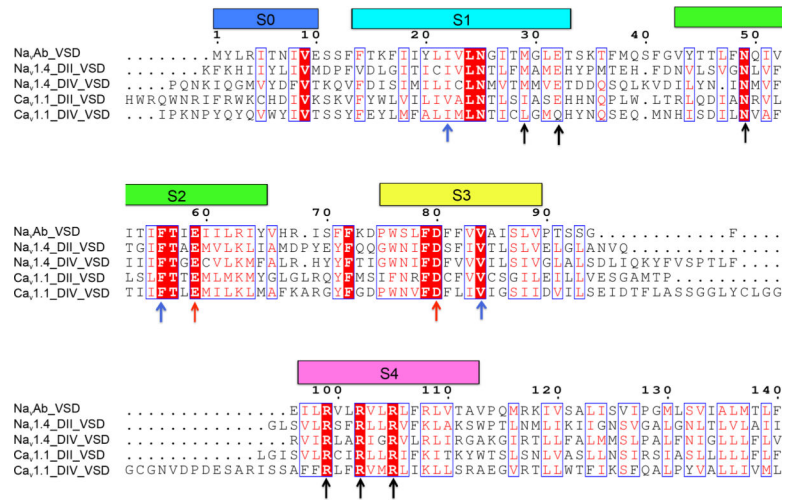
Extended Data Figure 1 |. Sequence alignment of Na$_v$Ab VS with human Na$_v$1.4 DII VS, Na$_v$1.4 DIV VS, Ca$_v$1.1 DII VS, and Ca$_v$1.1 DIV VS.

Colored rectangles represent TM helices. Black arrows indicate residues that form the guanidinium binding site, blue arrows indicate hydrophobic constriction site, and red arrows indicate the conserved intracellular negative cluster.
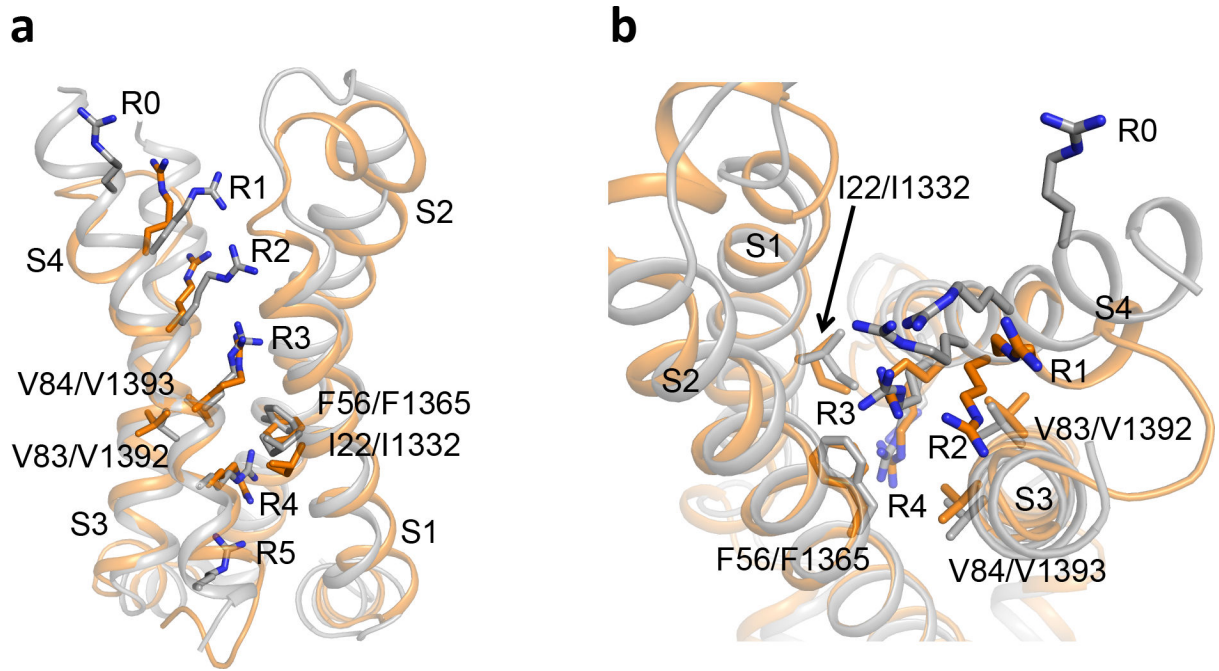
Extended Data Figure 2 |. Superposition of NavAb/WT VS and EeNa$_v$1.4 DIV VS.
a-b, Comparison of the conformations of Na$_v$Ab/WT VS (orange) and EeNa$_v$1.4 VSDIV (grey) in side view and top view, respectively. Arg sensors and hydrophobic residues in the HCS are labeled and shown side chain in sticks.

Extended Data Figure 3 |. Superposition of the VS between Na_vAb/WT and mutants.
a-b, VS structure alignment between Na_vAb/WT (grey) and NavAb/R3G (green) in side view and top view, respectively. **c-d**, VS structure alignment between NavAb/WT (grey) and Na_vAb/R2G (cyan) in side view and top view, respectively. Arg sensors and hydrophobic residues in the HCS are labeled and shown side chain in sticks.
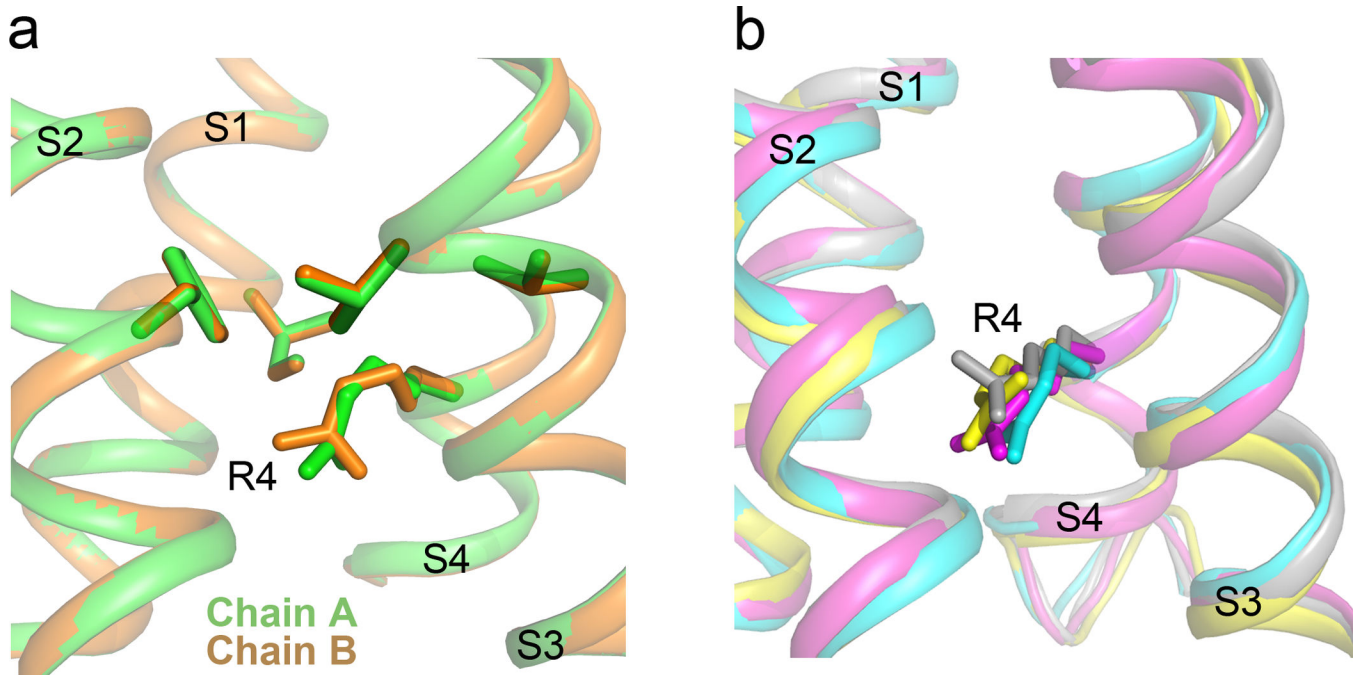
Extended Data Figure 4 |. R4 side chain conformational changes.
a, Different conformations of the R4 rotamer in Na_vAb/R3G Chain A (green) and Chain B (orange). **b,** Different conformations of the R4 rotamer in the four subunits of Na_VAb in the slow-inactivated state (PDB code 4EKW).
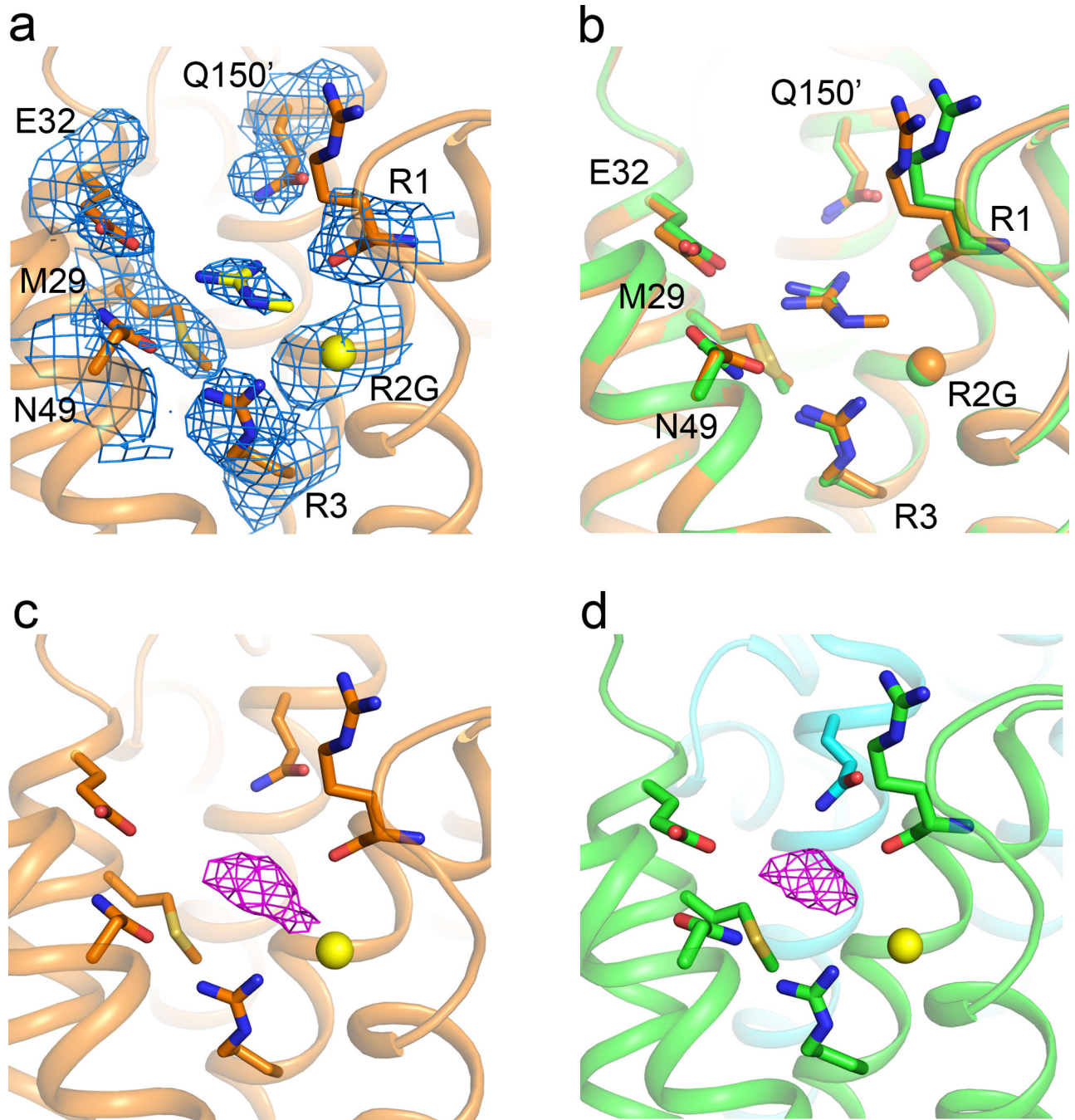
Extended Data Figure 5 |. Electron density maps for bound guanidinium and methylguanidinium ions.

a, 2mFo – DFc electron density map (blue mesh) of residues around the methylguanidinium binding site at 1σ. **b,** Overlay of guanidinium binding site (green) and methylguanidinium binding site (orange). **c-d,** Simulated annealing map (*Fo-Fc*) contoured at 3σ for methylguanidinium and guanidinium, respectively.

a

b
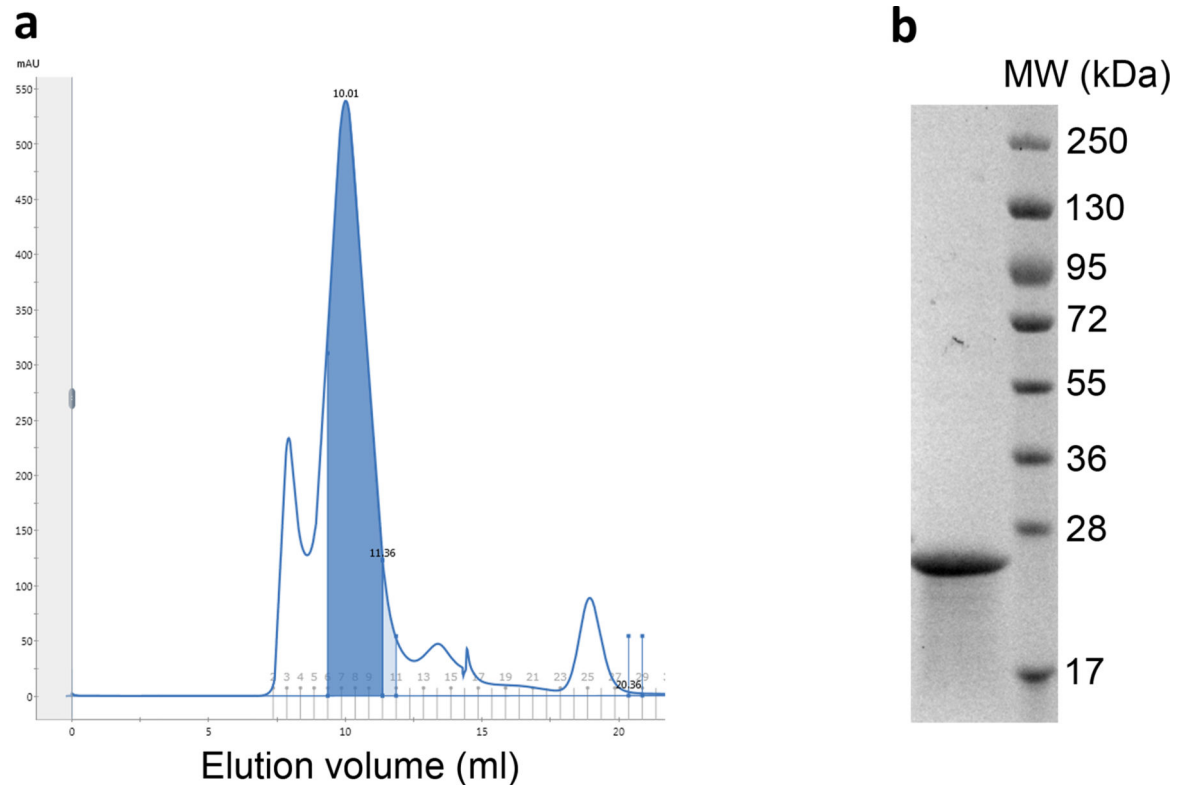
Extended Data Figure 6 |. Purification of Na$_V$Ab/R3G.
a, A representative gel-filtration chromatography of Na$_V$Ab/R3G, highlighted peak fractions were concentrated for crystallization. **b,** Concentrated sample was visualized on SDS-PAGE by Coomassie Blue staining.

Extended Data Table 1.

Data collection and refinement statistics.

	Na$_V$Ab/R3G	Na$_V$Ab/R2G Guanidinium	Na$_V$Ab/R2G Methyl Guanidinium	Na$_V$Ab/R2G Apo
Data collection				
Space group	*I222*	*I222*	*I222*	*P2$_1$22$_1$*
Cell dimensions				
a, b, c (Å)	126.8, 127.0, 192.3	126.6, 126.6, 191.8	126.3, 126.2, 191.6	125.5, 125.6, 192.0
α, β, γ (°)	90, 90, 90	90, 90, 90	90, 90, 90	90, 90, 90
Wavelength (Å)	0.99994	0.99994	0.99994	0.99994
Resolution (Å)	50–2.90 (3.00–2.90)	50–2.70 (2.80–2.70)	50–2.55 (2.64–2.55)	50–2.80 (2.90–2.80)
Rpim	4.6 (62.6)	4.0(62.0)	3.9 (64.0)	5.3 (58.1)
I/σI	16.6(1.5)	18.5 (1.2)	18.5 (1.0)	14.5 (0.8)
Completeness (%)	100 (99.9)	99.6 (96.5)	99.4 (95.0)	98.0 (81.6)
Redundancy	7.3 (7.2)	7.1 (5.4)	5.3 (3.8)	5.1 (3.2)

	Na$_v$Ab/R3G	Na$_v$Ab/R2G Guanidinium	Na$_v$Ab/R2G Methyl Guanidinium	Na$_v$Ab/R2G Apo
Refinement				
Resolution (Å)	42.50–2.86	42.31–2.70	42.31–2.52	48.46–2.90
No. reflections	35059	41173	51039	67766
R_{work}/R_{free}	21.25/23.99	20.98/24.59	20.31/22.66	23.35/26.03
No. atoms				
Protein	3606	3605	3673	7160
Ligand/ion	512	449	660	415
Water	0	5	35	0
B-factors				
Protein	108.7	97.8	103.1	112.89
Ligand/ion	128.2	107.5	130.8	115.8
Water		54.5	75.5	
R.m.s deviations				
Bond lengths (Å)	0.010	0.010	0.009	0.012
Bond angles (°)	1.311	1.215	1.253	1.703
Ramachandran plots				
Favored	93.2%	92.5%	94.0%	92.1%
Allowed	6.8%	7.3%	5.4%	7.4%
Outliers	0.0%	0.2%	0.6%	0.5%

Extended Data Table 2.

Statistical analysis of VS water occupancy from molecular simulations. Results of two-way t-tests on differences in average water count in 1 Å segments of the VS axial coordinate comparing WT and R3G simulations. In each segment, we compare the mean of 60 values (n=60, obtained from pooling the mean water counts of the four VS proteins from each of 15 simulation repeats). The HCS region (–5 to 1 Å, bold) has the largest effect size, indicating a region of biological significance.

Degrees of freedom	Axial Interval (Å,Å)	t-statistic	q value
	(−20,−19)	1.411	2.221 E-01
	(−19,−18)	2.878	1.024E-02
	(−18,−17)	4.389	7.674E-05
	(−17,−16)	4.802	1.696E-05
	(−16,−15)	4.545	4.465E-05
60+60−2	(−15,−14)	4.249	1.148E-04
	(−14,−13)	2.181	5.422E-02
	(−13,−12)	0.740	5.420E-01
	(−12,−11)	0.217	8.721 E-01
	(−11,−10)	2.760	1.276E-02

Degrees of freedom	Axial Interval (Å,Å)	t-statistic	q value
	(−10,−9)	4.283	1.078E-04
	(−9,−8)	−0.110	9.364E-01
	(−8,−7)	1.914	9.279E-02
	(−7,−6)	−5.668	4.626E-07
	(−6,−5)	−5.839	2.674E-07
	(−5,−4)	**−9.376**	**6.032E-15**
	(−4,−3)	**−12.075**	**9.500E-21**
	(−3,−2)	**−11.945**	**9.674E-21**
	(−2,−1)	**−10.018**	**2.422E-16**
	(−1,0)	**−5.812**	**2.674 E-07**
	(0,1)	**−7.910**	**1.027E-11**
	(1,2)	1.488	1.993E-01
	(2,3)	1.813	1.073E-01
	(3,4)	2.797	1.205E-02
	(4,5)	5.497	9.078E-07
	(5,6)	2.476	2.672E-02
	(6,7)	−3.688	8.593E-04
	(7,8)	−8.074	5.198E-12
	(8,9)	−3.257	3.462E-03
	(9,10)	−1.302	2.522E-01
	(10,11)	1.220	2.809E-01
	(11,12)	0.482	7.211 E-01
	(12,13)	−2.870	1.024E-02
	(13,14)	1.919	9.279E-02
	(14,15)	−0.003	9.978E-01
	(15,16)	0.887	4.569E-01
	(16,17)	1.843	1.044E-01
	(17,18)	1.319	2.522E-01
	(18,19)	0.263	8.686E-01
	(19,20)	0.249	8.686E-01

Supplementary Material

Refer to Web version on PubMed Central for supplementary material.

Acknowledgements

References

1. Venance SL et al. The primary periodic paralyses: diagnosis, pathogenesis and treatment. Brain 129, 8–17 (2006). [PubMed: 16195244]

2. Cannon SC Sodium channelopathies of skeletal muscle. Handb Exp Pharmacol (2017) doi: 10.1007/164_2017_52. [Epub ahead of print].

3. Sokolov S, Scheuer T & Catterall WA Gating pore current in an inherited ion channelopathy. Nature 446, 76–78 (2007). [PubMed: 17330043]

4. Struyk AF & Cannon SC A Na+ channel mutation linked to hypokalemic periodic paralysis exposes a proton-selective gating pore. J Gen Physiol 130, 11–20 (2007). [PubMed: 17591984]

5. Vicart S et al. New mutations of SCN4A cause a potassium-sensitive normokalemic periodic paralysis. Neurology 63, 2120–2127 (2004). [PubMed: 15596759]

6. Sokolov S, Scheuer T & Catterall WA Depolarization-activated gating pore current conducted by mutant sodium channels in potassium-sensitive normokalemic periodic paralysis. Proc Natl Acad Sci U S A 105, 19980–19985 (2008). [PubMed: 19052238]

7. Payandeh J, Scheuer T, Zheng N & Catterall WA The crystal structure of a voltage-gated sodium channel. Nature 475, 353–358 (2011). [PubMed: 21743477]

8. Catterall WA & Zheng N Deciphering voltage-gated Na^+ and Ca^{2+} channels by studying prokaryotic ancestors. Trends Biochem Sci 40, 526–534 (2015). [PubMed: 26254514]

9. Catterall WA, Goldin AL & Waxman SG International Union of Pharmacology. XLVII. Nomenclature and structure-function relationships of voltage-gated sodium channels. Pharmacol Rev 57, 397–409 (2005). [PubMed: 16382098]

10. Yan Z et al. Structure of the Nav1.4-beta1 complex from electric eel. Cell 170, 470–482 e411 (2017). [PubMed: 28735751]

11. Shen H et al. Structure of a eukaryotic voltage-gated sodium channel at near-atomic resolution. Science (2017).

12. Catterall WA Ion channel voltage sensors: structure, function, and pathophysiology. Neuron 67, 915–928 (2010). [PubMed: 20869590]

13. Starace DM & Bezanilla F A proton pore in a potassium channel voltage sensor reveals a focused electric field. Nature 427, 548–553 (2004). [PubMed: 14765197]

14. Sokolov S, Scheuer T & Catterall WA Ion permeation through a voltage-sensitive gating pore in brain sodium channels having voltage sensor mutations. Neuron 47, 183–189 (2005). [PubMed: 16039561]

15. Gamal El-Din TM, Scheuer T & Catterall WA Tracking S4 movement by gating pore currents in the bacterial sodium channel NaChBac. J of Gen Physiol 144, 147–157 (2014). [PubMed: 25070432]

16. Jurkat-Rott K, Groome J & Lehmann-Horn F Pathophysiological role of omega pore current in channelopathies. Front Pharmacol 3, 112 (2012). [PubMed: 22701429]

17. Moreau A, Gosselin-Badaroudine P & Chahine M Biophysics, pathophysiology, and pharmacology of ion channel gating pores. Front Pharmacol 5, 53 (2014). [PubMed: 24772081]

18. Wu F et al. A sodium channel knockin mutant (NaV1.4-R669H) mouse model of hypokalemic periodic paralysis. J Clin Invest 121, 4082–4094 (2011). [PubMed: 21881211]

19. Wu F et al. A calcium channel mutant mouse model of hypokalemic periodic paralysis. J Clin Invest 122, 4580–4591 (2012). [PubMed: 23187123]

20. Gosselin-Badaroudine P, Delemotte L, Moreau A, Klein ML & Chahine M Gating pore currents and the resting state of Nav1.4 voltage sensor domains. Proc Natl Acad Sci U S A 109, 19250–19255 (2012). [PubMed: 23134726]

21. Moreau A, Gosselin-Badaroudine P, Boutjdir M & Chahine M Mutations in the voltage sensors of Domains I and II of Nav1.5 that are associated with arrhythmias and dilated cardiomyopathy generate gating pore currents. Front Pharmacol 6, 301 (2015). [PubMed: 26733869]

22. Monteleone S et al. Mechanisms responsible for omega-pore currents in Cav calcium channel voltage-sensing domains. Biophys J 113, 1485–1495 (2017). [PubMed: 28978442]

23. Chakrabarti N et al. Catalysis of Na^+ permeation in the bacterial sodium channel Na_VAb. Proc Natl Acad Sci U S A 110, 11331–11336 (2013). [PubMed: 23803856]

24. Sokolov S, Scheuer T & Catterall WA Ion permeation and block of the gating pore in the voltage sensor of $Na_V1.4$ channels with hypokalemic periodic paralysis mutations. J Gen Physiol 136, 225–236 (2010). [PubMed: 20660662]

25. Payandeh J, Gamal El-Din TM, Scheuer T, Zheng N & Catterall WA Crystal structure of a voltage-gated sodium channel in two potentially inactivated states. Nature 486 135–139 (2012). [PubMed: 22678296]

26. Yarov-Yarovoy V et al. Structural basis for gating charge movement in the voltage sensor of a sodium channel. Proc. Natl. Acad. Sci. U.S.A. 109 E93–E102 (2012). [PubMed: 22160714]

27. Vargas E et al. An emerging consensus on voltage-dependent gating from computational modeling and molecular dynamics simulations. J Gen Physiol 140, 587–594 (2012). [PubMed: 23183694]

28. Catterall WA, Wisedchaisri G & Zheng N The chemical basis for electrical signaling. Nat Chem Biol 13, 455–463 (2017). [PubMed: 28406893]

29. Cooper KE, Gates PY & Eisenberg RS Diffusion theory and discrete rate constants in ion permeation. J Membr Biol 106, 95–105 (1988). [PubMed: 2465414]

30. Gamal El-Din TM, Martinez GQ, Payandeh J, Scheuer T & Catterall WA A gating charge interaction required for late slow inactivation of the bacterial sodium channel NavAb. J Gen Physiol 142, 181–190 (2013). [PubMed: 23980192]

31. Adams PD et al. PHENIX: a comprehensive Python-based system for macromolecular structure solution. Acta Crystallogr D Biol Crystallogr 66, 213–221 (2010). [PubMed: 20124702]

32. Emsley P & Cowtan K Coot: model-building tools for molecular graphics. Acta Crystallogr D Biol Crystallogr 60, 2126–2132 (2004). [PubMed: 15572765]

33. Chen VB et al. MolProbity: all-atom structure validation for macromolecular crystallography. Acta Crystallogr D Biol Crystallogr 66, 12–21 (2010). [PubMed: 20057044]

34. Petrek M, Kosinova P, Koca J & Otyepka M MOLE: a Voronoi diagram-based explorer of molecular channels, pores, and tunnels. Structure 15, 1357–1363 (2007). [PubMed: 17997961]

35. Jefferys E, Sands ZA, Shi J, Sansom MSP & Fowler PW Alchembed: a computational method for incorporating multiple proteins into complex lipid geometries. J Chem Theory Comp 11, 2743–2754 (2015).

36. MacKerell AD et al. All-atom empirical potential for molecular modeling and dynamics studies of proteins. J Phys Chem B 102, 3586–3616 (1998). [PubMed: 24889800]

37. Klauda JB et al. Update of the CHARMM all-atom additive force field for lipids: validation on six lipid types. J Phys Chem B 114, 7830–7843 (2010). [PubMed: 20496934]

38. Best RB et al. Optimization of the additive CHARMM all-atom protein force field targeting improved sampling of the backbone phi, psi and side-chain chi(1) and chi(2) dihedral angles. J Chem Theory Comput 8, 3257–3273 (2012). [PubMed: 23341755]

39. Jorgensen WL, Chandrasekhar J, Madura JD, Impey RW & Klein ML Comparison of simple potential functions for simulating liquid water. J Chem Phys 79, 926–935 (1983).

40. Noskov SY & Roux B Control of ion selectivity in LeuT: two Na^+ binding sites with two different mechanisms. J Mol Biol 377, 804–818 (2008). [PubMed: 18280500]

41. Venable RM, Luo Y, Gawrisch K, Roux B & Pastor RW Simulations of anionic lipid membranes: development of interaction-specific ion parameters and validation using NMR data. J Phys Chem B 117, 10183–10192 (2013). [PubMed: 23924441]

42. Abraham MJ et al. GROMACS: High performance molecular simulations through multi-level parallelism from laptops to supercomputers. SoftwareX, 1–7 (2015).

43. Darden T, York D & Pedersen L Particle mesh Ewald: An N·log(N) method for Ewald sums in large systems. J Chem Phys 98, 10089–10092 (1993).

44. Essmann U et al. A Smooth particle mesh Ewald method. J Chem Phys 103, 8577–8593 (1995).

45. Verlet L Computer "experiments" on classical fluids. I. thermodynamical properties of Lennard-Jones molecules. Phys Rev 159, 98–103 (1967).

46. Hoover WG Canonical dynamics: equilibrium phase-space distributions. Phys Rev A 31, 1695 (1985).

47. Nosé S A molecular dynamics method for simulations in the canonical ensemble. Mol Phys 52, 255–268 (1984).

48. Parrinello M & Rahman A Crystal structure and pair potentials: A molecular-dynamics study. Phys Rev Lett 45, 1196–1199 (1980).

49. Nosé S & Klein ML Constant pressure molecular dynamics for molecular systems. Mol Phys 50, 1055–1076 (1983).

50. Hess B P-LINCS: A parallel linear constraint solver for molecular simulation. J Chem Theory Comp 4, 116–122 (2008).

51. Torrie GM & Valleau JP Nonphysical sampling distributions in Monte Carlo free-energy estimation: Umbrella sampling. J Comp Phys 23, 187–199 (1977).

52. Roux B The calculation of the potential of mean force using computer simulations. Computer Phys Comm 91, 275–282 (1995).

53. Hub JS, de Groot BL & van der Spoel D g_wham-A free weighted histogram analysis implementation including robust error and autocorrelation estimates. J Chem Theory and Comp 6, 3713–3720 (2010).

54. McGibbon RT et al. MDTraj: A modern open library for the analysis of molecular dynamics trajectories. Biophys J 109, 1528–1532 (2015). [PubMed: 26488642]

55. Humphrey W, Dalke A & Schulten K VMD: visual molecular dynamics. J Mol Graph14, 33–38 (1996). [PubMed: 8744570]
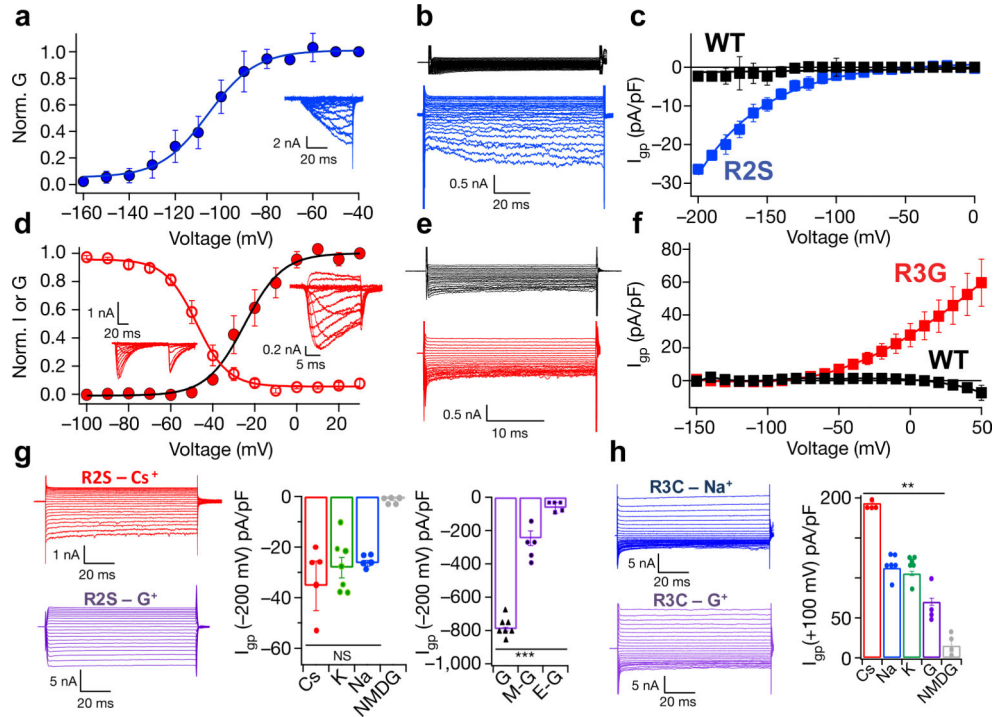
Figure 1: Functional properties of Na$_V$Ab/WT, Na$_V$Ab/R2S, and Na$_V$Ab/R3G.
a, Central pore Na$^+$ currents (inset) and G/V curve for Na$_v$Ab/R2S during 200-ms depolarizations from −200 mV to the indicated potentials. $V_{1/2}$= −105 ± 0.6 mV, k=10±0.9 (n=4). **b, c,** Gating pore Na$^+$ currents and I/V curves for Na$_v$Ab/R2S (blue) or Na$_v$Ab/WT (black) during depolarizations from −100 mV to the indicated potentials. n=10. **d,** Central pore Na$^+$ currents (inset) and G/V curve for Na$_v$Ab/R3G during depolarizations from-160 mV to the indicated potentials (filled circles; V_a=−24.8 ± 1.1 mV, k=9±1 (n=4)). Voltage dependence of steady-state inactivation (open circles) for Na$_v$Ab/R3G (V_h=−47.7±0.4 mV, k=7.5±0.3 (n=4)). **e, f,** Gating pore Na$^+$ currents and I/V curves for Na$_V$Ab/R3G (red) or Na$_V$Ab/WT (black) for voltage steps from 0 mV to the indicated potentials (n=11). **g,** Gating pore current through Na$_v$Ab/R2S for Cs$^+$ (n=5), K$^+$ (n=7), Na$^+$ (n=5), N-methyl-D-glucamine (NMDG, n=5), guanidinium (G, n=7), methylguanidinium (M-G, n=5), and ethylguanidinium, (E-G, n=5).. ***, P=0.00029. **h,** Gating pore current through Na$_v$Ab/R3C for Cs$^+$ (n=4), Na$^+$ (n=6), K$^+$ (n=6), G (n=4), and NMDG. (n=4). **, P=0.0011. Student's t-test, two-sided.
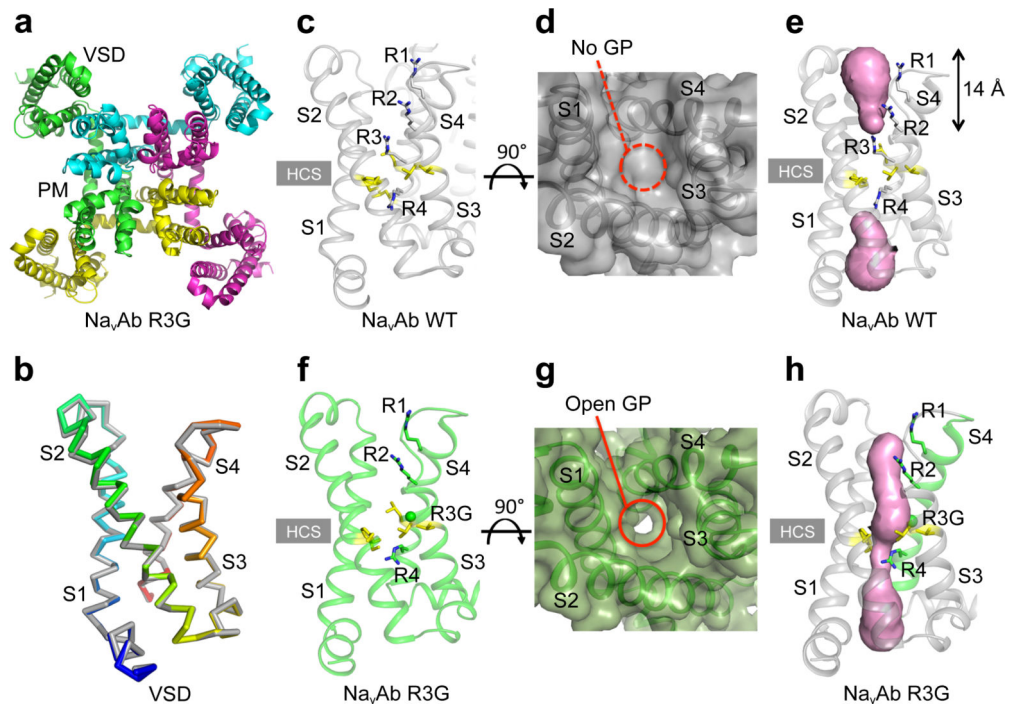
Figure 2. Structures of the VS of Na$_V$Ab/WT and Na$_V$Ab/R3G.
a, Structure of Na$_V$Ab/R3G in top view. **b,** Comparison of the conformations of Na$_V$Ab/WT (grey) and Na$_V$Ab/R3G (rainbow) VS in side view. **c-e**, Structures of NavAb/WT VS. (c) Side view highlighting gating charges in sticks. (d) Top view in spacefilling format. (e) MOLE2 analysis of water-accessible space in magenta. **f-h**, Structures of NavAb/R3G VS. (f) Side view highlighting gating charges. (g) Top view in spacefilling format. (h) MOLE2 analysis of water-filled space in magenta. Green balls in panels f and h indicate the positions of the missing sidechain of R3. In panels d and g, the dotted red line circles the position where the gating pore (GP) would be in the activated state and the solid red line circles the open GP. See Extended Data Table 1 for details.
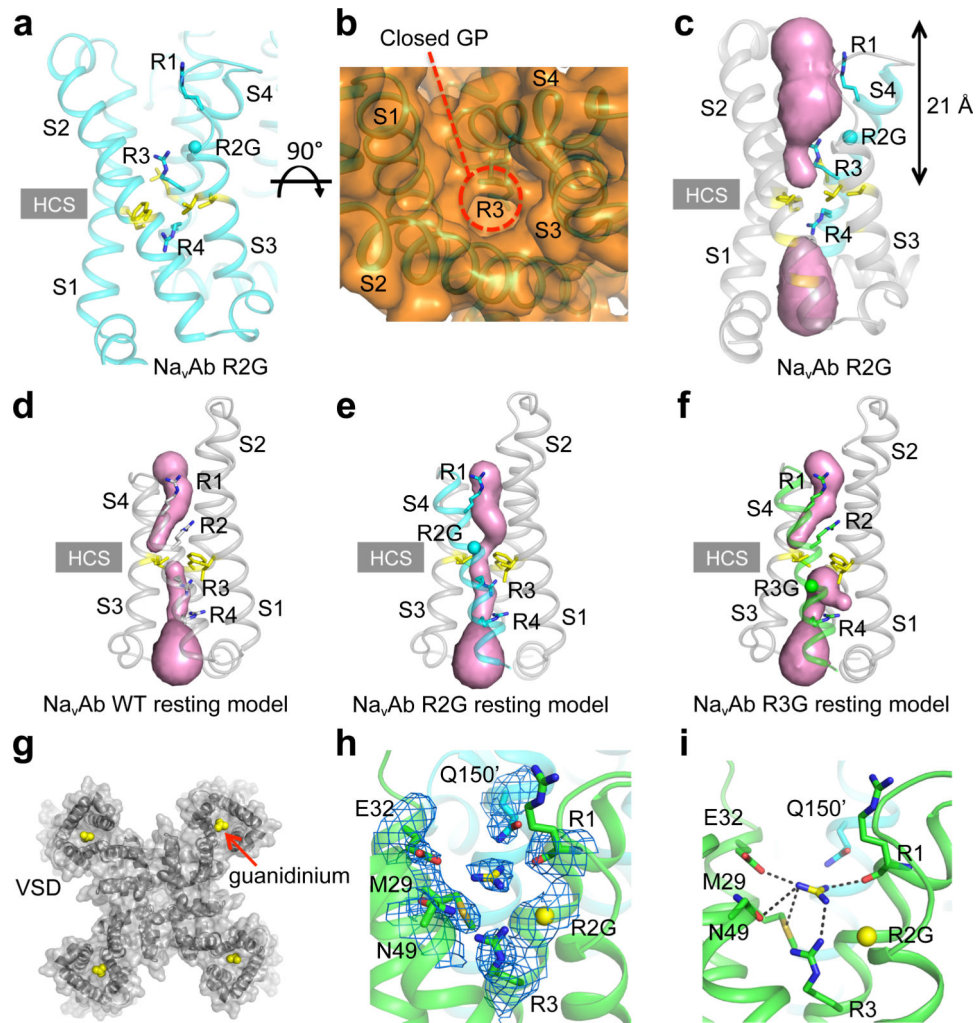
Figure 3. Structure of VS and guanidinium binding site of Na_VAb/R2G.
a-c, Structures of the activated VS of Na_VAb/R2G. (a) Side view with gating charges highlighted in sticks. (b) Top view in spacefilling format. The dashed red line indicates the position of the closed gating pore (GP) (c) MOLE2 analysis of water-filled space in magenta blobs. **d-f.** Rosetta structural models of Resting State 2 of the VS were re-optimized with the amino-acid sequence of Na_VAb for Na_VAb/WT (d), Na_VAb/R2G (e), and Na_VAb/R3G (f). The perspective is rotated ~180° around the vertical axis to better illustrate the arginine gating charges in Resting State 2. Green balls represent missing arginine side chains of R2 and R3, respectively. Magenta blobs represent solvent accessible volume modeled with MOLE2. **g,** Top view of Na_VAb/R2G with one guanidinium bound to each VS. **h,** 2mFo – DFc electron density map (blue mesh) of residues around the guanidinium binding site at 1σ. **i,** Interaction network between guanidinium and amino acids in the VS of Na_VAb/R2G. Grey dashed lines show interatomic distances shorter than 4 Å. See Extended Data Table 1 for details.
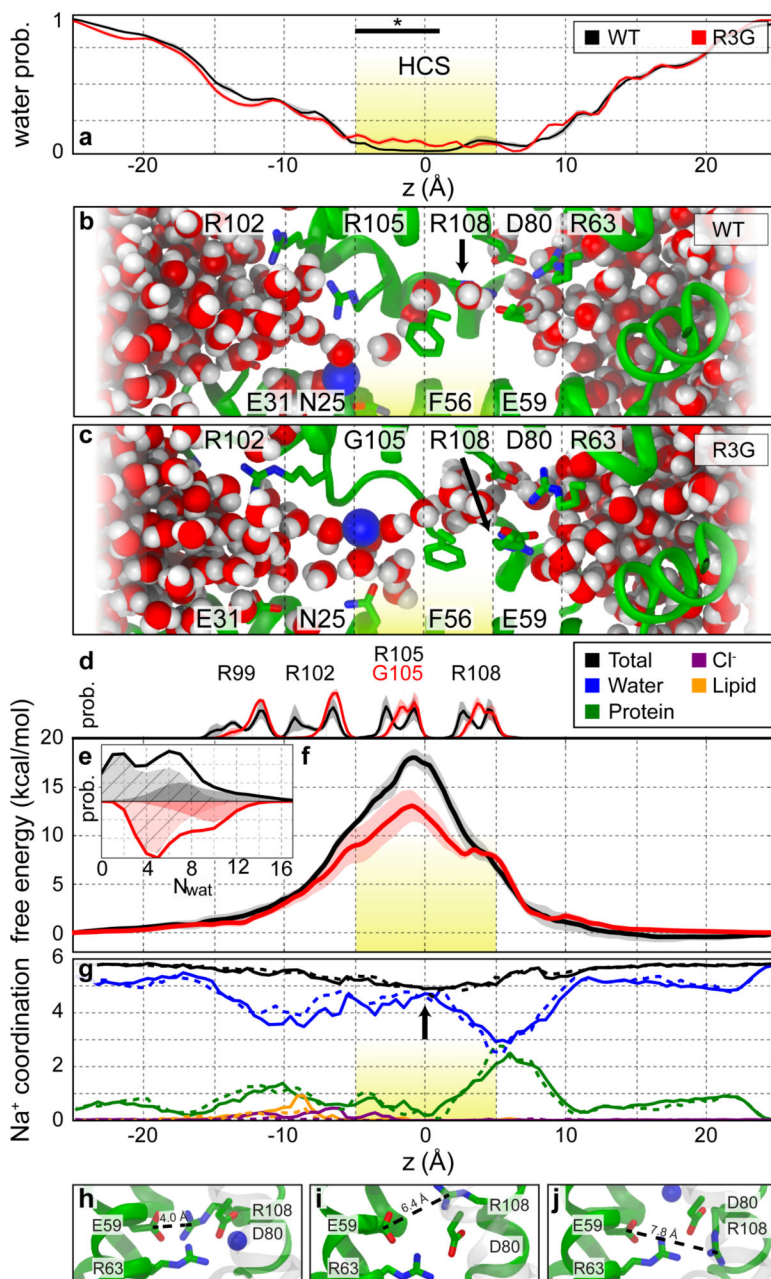
Figure 4. R3G mutation lowers the free energy barrier for Na$^+$ conductance.
a, Probability distribution of water along the domain axis for Na$_v$Ab/WT (black) and Na$_v$Ab/R3G (red). **b and c**, Representation of VS from Na$_v$Ab/WT and Na$_v$Ab/R3G simulations where Na$^+$ (blue sphere) is restrained at z = −5 Å. The S2 segment (residues 45–65) is omitted for clarity. **d**, Axial distribution of gating charge Cα for Na$_v$Ab/WT and Na$_v$Ab/R3G. The axial position in the crystallographic structure is shown as a vertical line. **e**, Probability distribution of water in the HCS (−5 Å to 5 Å) across all simulations of WT (black) and R3G (red). The total probability is separated into frames where Na$^+$ occupied the hydrophobic constriction (solid) or was outside this region (cross-hatched). **f**, Potential of mean force for Na$^+$ conduction within the Na$_v$Ab/WT (black) and Na$_v$Ab/R3G (red) pore

computed using umbrella sampling. Yellow highlights the HCS. **g**, Average coordination of Na^+ as a function of ionic position along the VS principal axis, for Na_vAb/WT (solid lines) and Na_vAb/R3G (dashed lines). The first coordination shell of Na^+ is partitioned for coordination to protein (green), water (blue), lipid headgroups (orange), and counterions (purple). **h-j,** Representative snapshots from Na_vAb/R3G simulations depicting R4 conformational isomerization. *, P<0.002, n = 60; see Extended Data Table 2 for details.